Global and Planetary Change 203 (2021) 103544

Contents lists available at ScienceDirect

Global and Planetary Change

journal homepage: www.elsevier.com/locate/gloplacha

Research Article

Tectonic geomorphology and active faults in the Bolivian Amazon

Umberto Lombardo[a,*], Christoph Grützner[b]

[a] Institute of Geography, University of Bern, Hallerstrasse 12, Bern 3012, Switzerland
[b] Institute of Geological Sciences, Friedrich-Schiller-Universität Jena, Burgweg 11, Jena 07749, Germany

ARTICLE INFO

Keywords:
Bolivia
Amazon basin
Forebulge
Active fault
Landscape evolution

ABSTRACT

The Bolivian Amazon foreland basin is controlled by i) the sediment input from the Andes and the topographic load; ii) the basinal uplift in the forebulge; and iii) the uplifting Fitzcarrald Arch in the north. These boundary conditions should lead to bending and active faulting of the crust. However, although the presence of active faults has been inferred from geomorphological studies, neither seismicity studies nor geodetic methods and geomorphological constraints have been successful in identifying active faults so far. Reasons for this are mainly the dense vegetation and the extremely dynamic fluvial landscape of the Bolivian Amazon. In this study we use the TanDEM-X and SRTM digital elevation models to show that there are at least five faults, several tens of kilometres long, that are active. We present offset measurements from fault scarps and combine these data with river system analyses. Our results suggest that tilting of tectonic blocks occurred in the Late Pleistocene or Holocene. The reversal of fluvial longitudinal profiles and incipient creek erosion inside paleochannels, markers of young tectonic activity, allow us to reconstruct the tilting directions. We find two orthogonal main faulting directions: WNW-ESE trending faults parallel to the Andean uplift and NNE-SSW trending faults tangent to the bulge of the uplifting Fitzcarrald Arch. Thus, our study area records the interplay between these two main drivers of crustal deformation. We show that some fault scarps were caused by large single earthquakes with magnitudes of around M_W7, while others have recorded multiple strong seismic events. These magnitudes exceed by far the magnitudes known from instrumental seismicity in the last 40 years. Our results shed light on the seismic hazard of the region and highlight that catastrophic river course changes due to sudden uplift in this low-relief region are an underestimated hazard.

1. Introduction

The Llanos de Moxos (LM) in the Bolivian Amazon is a seasonally flooded savannah that covers most of the southern Amazonian foreland basins (Fig. 1). With a total area of about 100,000 km^2 it is among the largest wetlands of South America (Junk, 2013). Recent studies have shown that this region, inhabited since the early Holocene, is one of the early Holocene world centres of plant domestication (Lombardo et al., 2020). The landscape of the LM is characterized by a dense network of rivers and paleorivers that criss-crosses the alluvial plains of the Beni and Mamoré Rivers. These, together with the Iténez (Guaporé in Brazil) and the Madre de Dios, form the Madeira, the largest tributary to the Amazon River. The LM is extremely flat, with a general slope of 10 cm per kilometre. The low slope makes the fluvial network of the LM very active, with high depositional rates associated to frequent river avulsions and the formation of crevasse splays (Lombardo, 2016). River behaviour and flooding patterns are mostly controlled by precipitation and the general slope. Changes in slope, as those that could occur following seismic events, can induce river avulsion (Schumm et al., 2002; Smith et al., 1997; Timár et al., 2005) and can be potentially catastrophic, as rivers that suddenly change their course could lead to wide-spread flooding. For example, the Mississippi River shortly reversed during the New Madrid Earthquakes (Fuller, 1988). It is very difficult to assess the likelihood of a similar scenario in the LM, because both historical and instrumental seismicity is low. In our study area, strong subduction earthquakes occurred in depths of 550–650 km (Dziewonski et al., 1981; Ekström et al., 2012), but only six crustal events with magnitudes <M5.0 have been recorded since the 1980s (USGS, 2020; Table 1; Fig. 2). Neither can these crustal events be tied to causative faults, nor were they strong enough to produce a surface rupture. Also, they were not strong enough to be studied in detail by teleseismic body-waveform analyses. Publicly available data from the regional seismic network shows no seismicity in the study area in the past twelve months, although the station coverage is sparse. The map of

---

* Corresponding author.
E-mail address: umberto.lombardo@giub.unibe.ch (U. Lombardo).

https://doi.org/10.1016/j.gloplacha.2021.103544
Received 6 January 2021; Received in revised form 14 June 2021; Accepted 14 June 2021

the seismic risk in Bolivia identifies the LM as a no-risk area (Observatorio_San_Calixto, 2019). No dense GPS network is available that would allow for detailed insight into active tectonics. Similarly, no geodetic studies on long-term or short-term crustal deformation are available for the Llanos de Moxos. Drainage networks, catchments, and stream profiles have been used to analyse active tectonics. Mostly, these studies focus on mountainous areas or highly active regions (El Hamdouni et al., 2008; Snyder et al., 2000). Landscapes with very low relief, such as the LM, are difficult to assess because the low relief requires high-resolution topography data covering large areas. However, the effects of even small vertical crustal motion on the drainage network can be significant. Tectonic activity during the Holocene in the LM has been inferred by the analysis of several elements of its landscape. The large lake Rogoaguado, part of a group of lakes created by neotectonic activity along the "Línea Bala-Rogagua" in the northern part of the LM (Dumont and Fournier, 1994; Hanagarth, 1993; Fig. 1), formed inside a former Beni River floodplain because of the reversal of its longitudinal floodplain profile about ca. 5850 cal yrs. BP (Lombardo, 2014). The Mamoré River, which drains most of the LM and which is the largest tributary to the Madeira, shows asymmetric and compressed meanders together with changes in slope and sinuosity index. This indicates that its course has been influenced by neotectonic events (Hanagarth, 1993; Lombardo, 2014). Identifying active faults could help understand the processes underlying the evolution of the basin and assess the seismic hazard in the region.

It is very difficult to assess earthquake recurrence intervals, fault activity, paleo-earthquake magnitudes, and uplift rates based on these geomorphological traces. On the contrary, the identification and paleoseismic study of fault scarps, which are the direct surficial expression of faults, can provide those estimates with good confidence (Grützner et al., 2017; Lin et al., 2006; Swan III et al., 1980). Fluvial deposits associated to fault scarps have provided very high-resolution records of past seismic events, allowing a precise estimation of recurrence time (Berryman et al., 2012). These studies are needed in the LM, where the record of past earthquakes is extremely limited. In the Bolivian Amazon, fault scarps in the alluvial plains have never been identified before. Here, we present new data derived from the analysis of the digital elevation models TanDEM-X and SRTM that show the presence of at least five faults crossing the Bolivian Amazon. The implication of

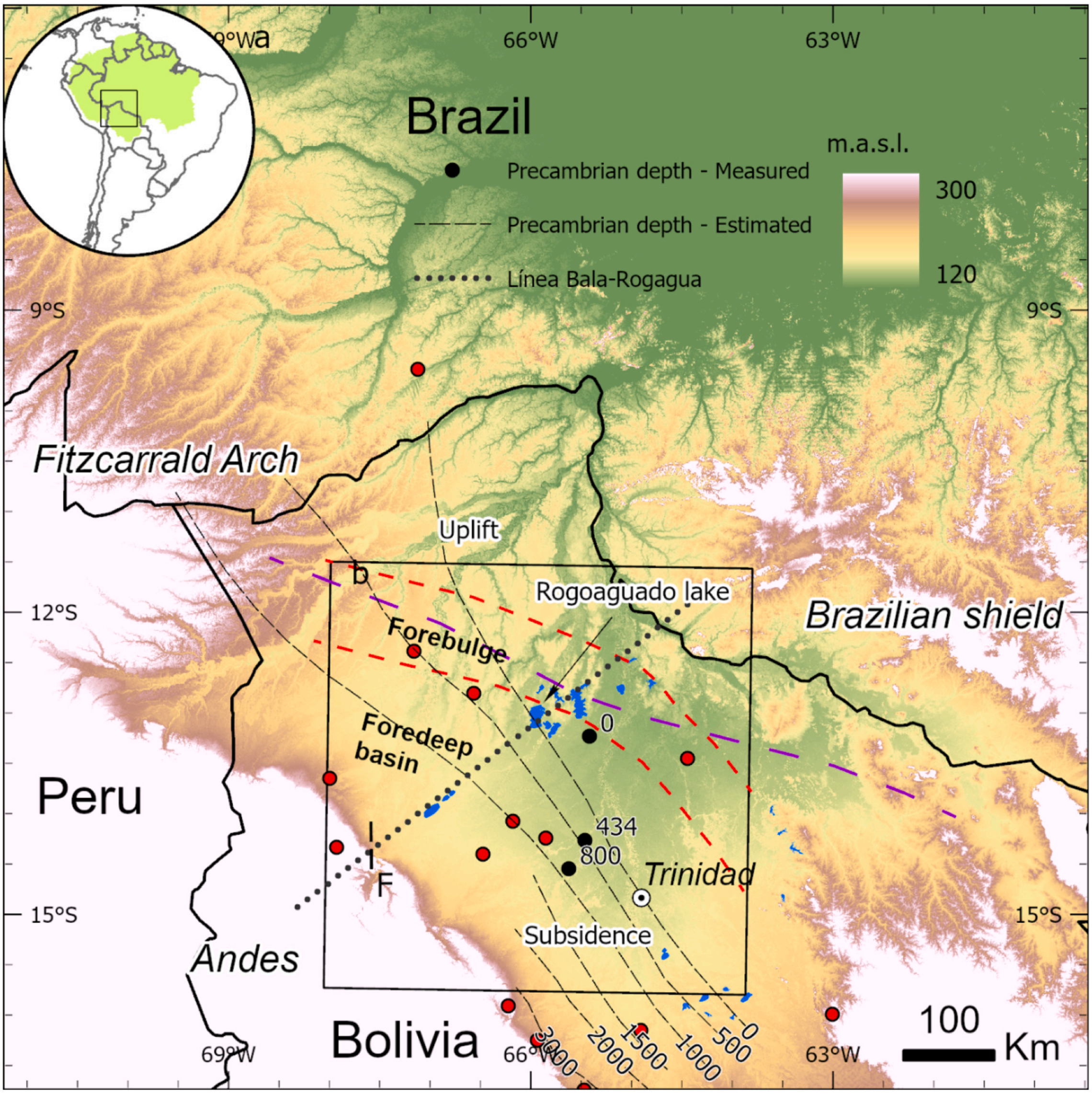

Fig. 1. General setting of the Llanos de Moxos. Depth of the Precambrian basement and location of the Línea Bala-Rogagua based on Hanagarth (1993). Approximate location of the foredeep and forebulge is based on Aalto et al. (2003) (red dashed lines) and Roddaz et al. (2006) (violet dashed line). The red dots are shallow (<45 km deep) earthquakes in the past 40 years with magnitudes between M4 and M5 (USGS, 2020). Vertical line "F" is a fault identified in Dumont (1996). Inset b shows the study area (Fig. 2). (For interpretation of the references to colour in this figure legend, the reader is referred to the web version of this article.)

these faults in terms of basin geodynamics, landscape evolution, fluvial dynamics, and seismic hazard are discussed.

1.1. *Geological setting*

The LM is a large floodplain made of unconsolidated sediments overlaying the Precambrian basement, lithological changes within the LM are restricted to small and localized outcrops of pre-Cambrian basement mostly located in the eastern part of the LM (Fig. 2). The floodplains that constitute the LM are enclosed by a triangle formed by the Andes along the SW border, the Brazilian shield to the east, and the southern margin of the Fitzcarrald Arch to the north (Fig. 1). They constitute the southern Amazonian foreland basin, with the foredeep of the basin subsiding because of the sedimentary load and basinal uplift in correspondence with the forebulge (DeCelles and Giles, 1996). The location of the forebulge, shown in Fig. 1, has been estimated by GPS surveys of longitudinal river gradients (Aalto et al., 2003; Roddaz et al., 2006). This geological setting is complicated by the uplift of the Fitzcarrald Arch. This is a broad foreland uplift caused by the flat slab subduction of the oceanic Nazca Ridge. It separates the southern Amazonian foreland basin, which largely overlaps with the LM, from the northern Amazonian foreland basin (Espurt et al., 2007; Regard et al., 2009; Roddaz et al., 2005). Instead of sinking into the mantel, the Nazca oceanic crust forms a flat-slab: a segment of oceanic crust that moves almost horizontally below the continental crust. Geophysical studies have shown that the depth of the earthquakes along the flat slab subduction zone goes from 80 km over the axis of the flat-slab to 150 km towards the borders, where the slab tears down and re-initiates normal subduction (Antonijevic et al., 2015; Bishop et al., 2017). The exact mechanism for how the flat slab induces the formation of the Fitzcarrald arch is however still debated (Bishop et al., 2018). In fact, the flat slab re-initiates normal subduction in correspondence of the eastern margin of the Andes plunging at a high angle (~70°) into the mantle before reaching the Fitzcarrald Arch (Antonijevic et al., 2015; Bishop et al., 2018). However, it is possible that the flat-slab scraped the bottom of the continental lithosphere and pushed that material forward, inducing the bulge that constitutes the Fitzcarrald Arch (Axen et al., 2018). The flat-slab also induces pronounced subsidence in the surrounding basins (Espurt et al., 2007). Therefore, the LM is under two contrasting forces: uplift in the north resulting from the push of the Nazca flat-slab which likely overlaps with a large part of the forebulge; and subsidence in the south resulting from compaction of the deposited sediments, the loading of the edge of the continental lithosphere by the overriding orogenic belt (Dumont, 1996), and the subsidence induced by the flat slab (Espurt et al., 2007). This setting is consistent with several field observations. Rivers deposit most of their sedimentary load in the central and southern LM, in which the accommodation space is provided by compaction and subsidence (Lombardo, 2016). Pre-Cambrian rocks crop out in the north of the LM (Hanagarth, 1993; Fig. 2), while the basement is found under 800 m of unconsolidated sediments in the central LM and at a depth of 3000 m along the edge of the sub-Andean zone (Plafker, 1964; Fig. 1).

The stress field in the LM is poorly understood. The World Stress Map (Heidbach et al., 2018; Heidbach et al., 2016) shows a general trend of SW-NE directed maximum horizontal stresses (S_{Hmax}) based on earthquake data and borehole breakouts, associated with reverse faulting. Assumpção et al. (2016) analysed earthquake focal mechanisms to map the intraplate stress field in South America. They report (W)SW-(E)NE directed S_{Hmax} in the entire Amazon Basin that lead to reverse faulting. However, the data gap in our study area due to the lack of earthquakes may obscure regional details. Norabuena et al. (1998) show that ~E-W directed GPS velocities, with respect to stable South America, prevail in our study area, but the number of stations in the LM is insufficient to provide detailed information on whether or not the LM is in a regime of shortening or extension. Thus, it remains unclear if the LM is under the ~(W)SW-(E)NE compressive stress field or if it undergoes regional extension due to a bending lithosphere in a forebulge setting.

2. Methods

Neotectonic features of the LM have been identified using a mosaic of 15 TanDEM-X tiles covering the central and northern LM. The TanDEM-X data have a spatial resolution of 0.4 arcseconds, which roughly corresponds to 12 m (raster size) in our study area (Esch et al., 2012), and 2 m relative vertical accuracy (4 m absolute vertical accuracy). Land cover has been assessed based on Landsat 8 imagery accessed via GLOVIS (https://glovis.usgs.gov/) using the (6,5,2) band combination. To enhance the expression of small vertical changes within the general landscape, the TanDEM-X mosaic has been represented using a rainbow-like colour scale and image stretching. A de-trended image has been visually analysed to detect slope inversions along paleochannels, which have been interpreted as evidence of tilting blocks. First, 1170 points have been randomly placed over the savannah in order to extract the

Table 1
List of Earthquakes provided by Observatorio San Calixto (personal communication).

Date	Latitude	Longitude	Depth (km)	Magnitude type	Magnitude
02/01/1988	−16.14999962	−64.91000366	12	M	4.1
03/07/1996	−13.45230007	−64.44619751	35	mL	4.1
05/02/1997	−14.24300003	−65.84999847	33		3.9
06/11/1996	−9.590000153	−67.12000275	0	mb	4.2
07/04/1997	−12.80799961	−66.56900024	0	mL	4.5
07/12/2006	−15.9076004	−66.22100067	35	ML	4
08/08/1994	−13.87769985	−68.28479767	603	mb	5.4
09/06/1994	−13.80249977	−67.58809662	638	mb	7.1
09/06/1994	−13.9321003	−68.04029846	640	mb	5.9
09/06/1994	−14.00829983	−67.28469849	638	mb	5.2
10/06/1994	−13.99269962	−67.5196991	639	mb	4.2
11/07/1988	−16.2493	−65.93139648	35	M	4.6
12/05/2012	−17.96899986	−63.1609993	5		3.1
12/09/2019	−15.39420033	−64.85119629	585		5.7
13/01/1988	−13.64999962	−68	15	M	4.1
14/03/1995	−15.19110012	−64.86260223	585	mb	5.6
18/05/1978	−14.07299995	−66.1780014	33		4.9
21/03/1996	−14.33600044	−67.9285965	35	mb	4.7
22/06/1996	−12.39000034	−67.16000366	0	mL	4.6
22/11/2011	−15.36400032	−65.08999634	550		6.6
23/06/1994	−13.95429993	−67.09580231	650	mb	4.5
25/08/2018	−14.40079975	−66.4756012	16		4.1
28/03/2004	−16.74799919	−65.47100067	30	mb	4
31/12/1987	−15.98999977	−63.00999832	44	M	4

elevation values while minimizing the elevation error due to the presence of forest (Lombardo et al., 2012; Fig. 3). Then, a trend surface has been interpolated with the Trend tool in ArcGIS with a 12th order polynomial using the elevation values of the savannah. The de-trended image has been obtained by subtracting the trend surface from the original DEM. The de-trended DEM shows the elevation anomalies with respect to the average elevation, therefore making the tilting of the paleochannels more evident (Zhang et al., 2020) All analyses have been performed with ArcGis 10.7. The rotation angle of the tilting blocks has been calculated by analysing the present-day slope of the paleochannel. Given 2 points, A and B, along the paleochannel, the rotation angle has been calculated as arctan (DH/DX), where DH is the difference in elevation between point A and B along the paleochannel measured in the de-trended DEM and DX is the along channel distance between A and B (Fig. 4). Profiles across the fault scarps have been produced using the Cosi-Corr package (Leprince et al., 2007). The number of pixels used as parameters for the topographic profiles are: stack length 501, stack width 31, and stack spacing 32 for faults 1, 2, and 3 using the TanDEM-X data. For additional measurements using SRTM data we chose stack length 101, stack width 21, and stack spacing 22 for fault 5. Stack length is about 3 km long on each side of the fault in order to have profiles long enough to discard those parts of the profile that are covered with forest. By doing so, the calculation of the vertical offset across the scarps is based on those parts of the landscape that are covered with savannah only. Fig. 5 shows an example of a topographic profile across fault 5 where the offset has been measured only from the part of the profile without forest cover.

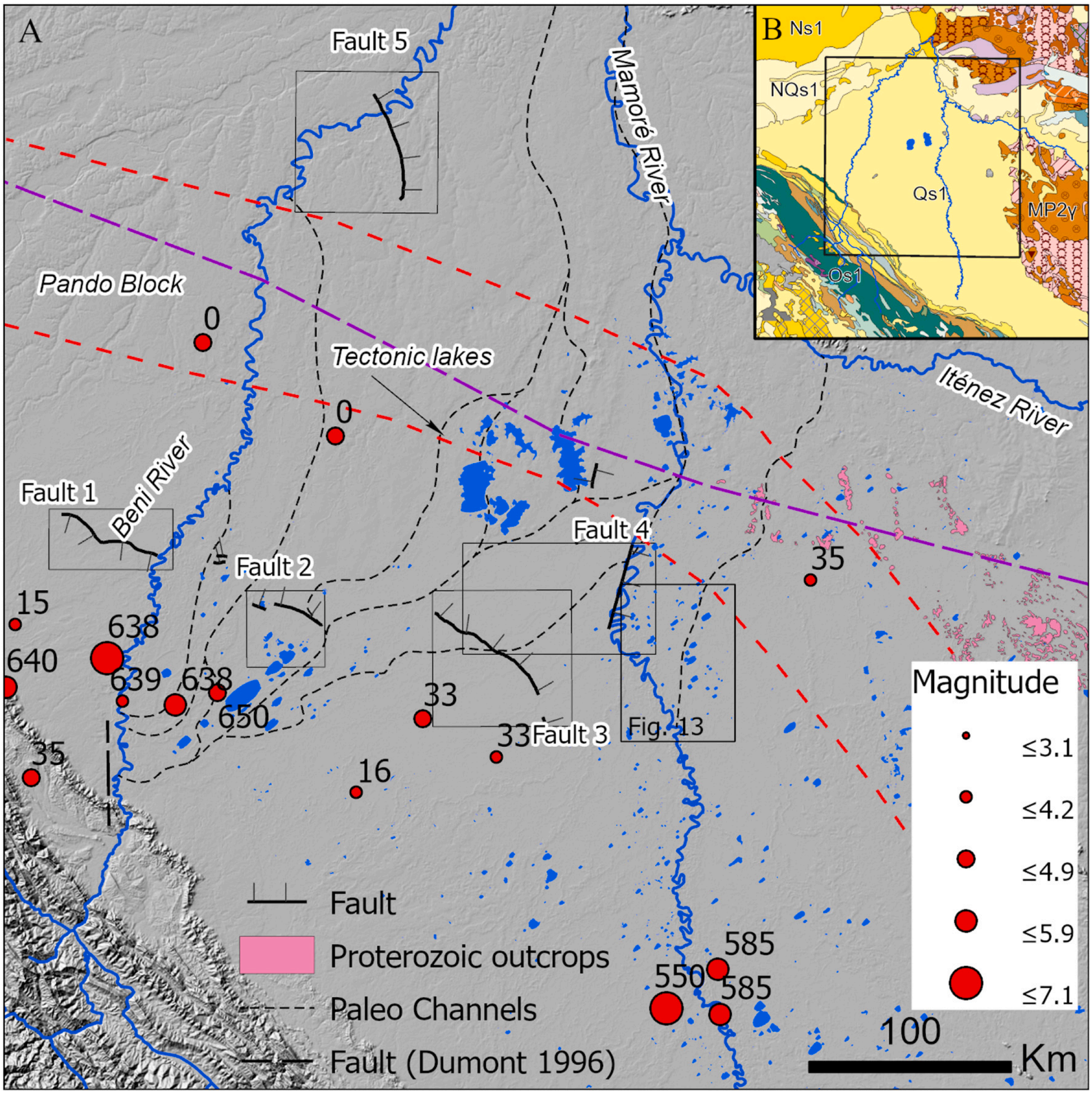

Fig. 2. A) Study area. Hill shade of the SRTM DEM with location of the studied faults (solid black lines; note that ticks mark the downthrown block and do not necessarily imply normal faulting). Black dashed lines indicate river paleo courses, blue lines are the major active rivers. The red dots are earthquakes, size is proportional to the magnitude, the label of the red dots is the depth of the earthquake in km. Earthquakes have been assembled by combining the database of the Bolivian Observatorio San Calixto (Table 1) and the USGS dataset (USGS, 2020). Red and violet dashed lines represent the location of the forebulge as in Fig. 1. B) Geologic map of the study area (Gómez et al., 2019). Only the main chronostratigraphic units are labelled: Qs1: Quaternary sedimentary siliciclastics; NQs1: Neogene-Quaternary sedimentary siliciclastics; Ns1: Neogene sedimentary siliciclastics; MP2γ: Mesoproterozoic plutonic granitics; Os1: Ordovician sedimentary siliciclastics. All the faults are located within the same Qs1 unit, which is made of unconsolidated sediments of fluvial origin. (For interpretation of the references to colour in this figure legend, the reader is referred to the web version of this article.)

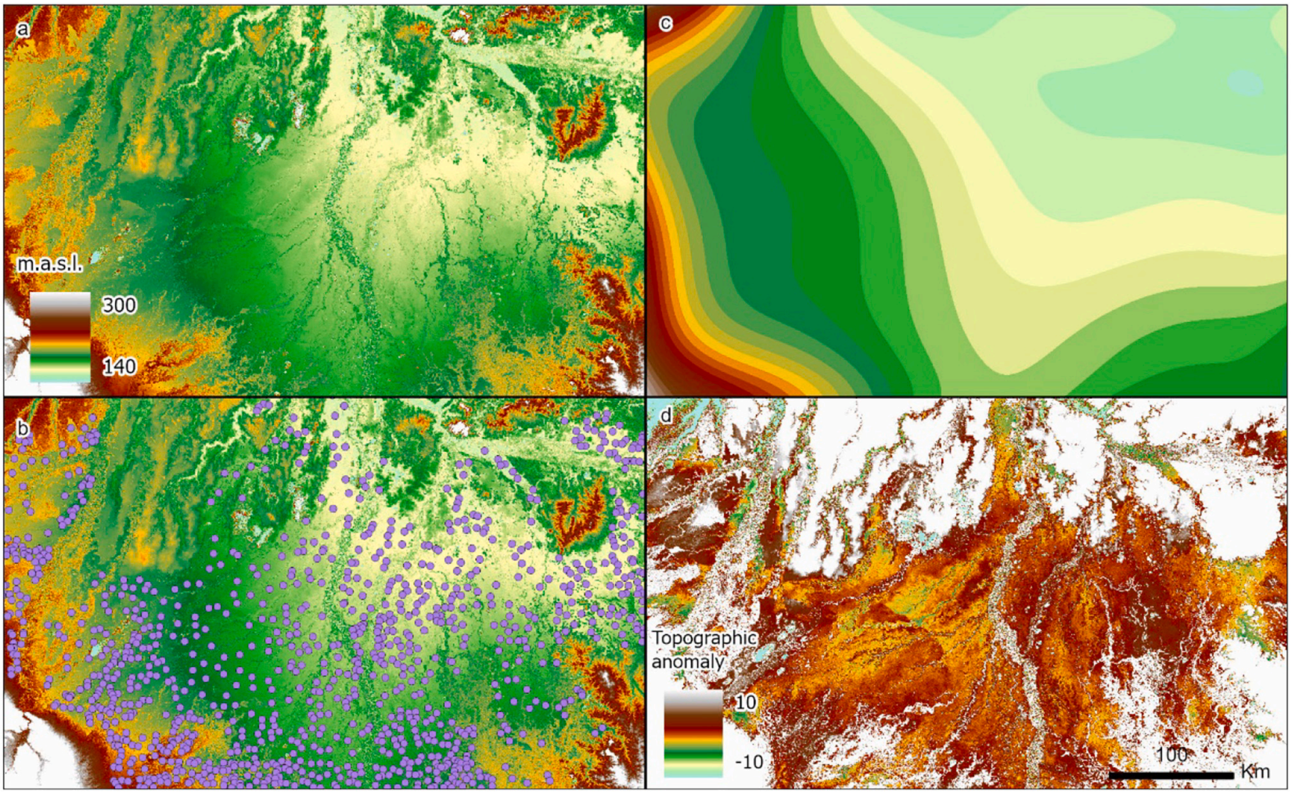

Fig. 3. DEM processing. In a the original DEM; In b points randomly placed over the savannah; in c trend surface interpolated from the DEM value associated to each of the points in b; d de-trended DEM derived from the original DEM (a) minus the trend surface (c).

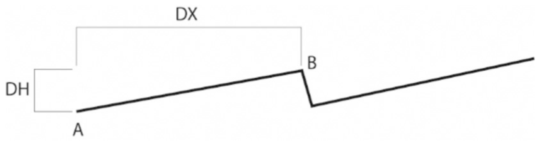

Fig. 4. Calculation of the rotation of the tilted blocks. The thick line is a representation of the topographic profile of a paleochannel as seen in the de-trended image. The rotation is the arctan of DH/DX.

3. Results and interpretation

3.1. Location and geometry of the faults

Four active faults, visible as kilometre-scaled lineaments, have been identified by visual analysis of the TanDEM-X digital elevation model and by the analysis of topographic profiles. All of them are located in the western part of the LM (Fig. 2). The fault scarps become visible in the DEM once rainbow-like colour scale is applied and the image is stretched. An additional fault (fault 4) running through an active flood plain was previously inferred from the elevation difference of the left and right river banks of the Mamoré river and from changes of its planform (Lombardo, 2014).

The westernmost fault (fault 1 in Figs. 2 and 6) is located on the western side of the Beni River. This lineament is 50 km long and runs NW-SE. The northern block is elevated and the scarp faces towards the SW (Fig. 6a). Vertical offset measurements along strike show an asymmetric triangular pattern with a maximum vertical offset of around 4 m 7 km from the eastern end of the fault (Fig. 6d). The vertical offsets do not increase continuously until they reach the maximum value but show deviations of up to two metres from the general trend. This offset distribution is within the observed ranges documented in the literature (e.g., Barka et al., 2002; Bürgmann et al., 1994; Haeussler et al., 2004; Scholz, 1982). Fault 1 is followed by the forest-savannah ecotone for most of its length. A series of s-shaped elongated lakes border the fault (Fig. 6c), resembling en-echelon fractures that form in shear zones (Choi et al., 2018; Quigley et al., 2010; Shen and Rogozhin, 2018). Their angle is about 45° with respect to the main fault trend. Thus, we interpret them as tension fractures rather than Riedel shears (Fig. 6; Bartlett et al., 1981; Riedel, 1929; Tchalenko, 1970; Tchalenko and Ambraseys, 1970). This indicates that the fault has a significant left-lateral component where it is striking ~E-W. No such features were found along the NW-striking sections of the fault. We found no markers that would allow for precisely measuring single-event lateral offsets or cumulative horizontal displacements. At its NW tip the fault appears to left-laterally offset an NE-SW elongated ridge, but due to the dynamic river system no suitable markers are preserved and we refrain from quantitatively interpreting a potential lateral component of motion. The rather sinuous fault trace is not typical of pure strike-slip faults, which tend to be straight in map view due to their usually steep or vertical dip (e.g., the San Andreas Fault in California, the Altyn Tagh Fault in China, the North Anatolian Fault in in Turkey, the Dzhungarian and Chilik Faults in Kazakhstan, the Dinaric strike-slip faults in Slovenia, etc.). However, such curvature is known from dip-slip faults. Thus, we interpret fault 1 as a dip-slip fault based on its sinuous surface trace and on the typical distribution of the vertical offset. Along its E-W trending section, a left-lateral component of motion is likely. The plateau in vertical throw between 10 and 30 km along strike could also indicate that a significant portion of the total slip is taken up by left-lateral motion (Fig. 6).

Further to the east, we find a second fault scarp within the fan of the Beni River (Fault 2 in Fig. 7), which runs perpendicular to the river channels. Fault 2 is 25 km long and strikes NW-SE. It is almost a continuation of fault 1, but runs slightly further to the SW. The fault scarp faces towards the NE and the southern block moved up relative to the northern one. We measured a maximum vertical displacement of about 8 m at about a third of the fault's length from its eastern tip.

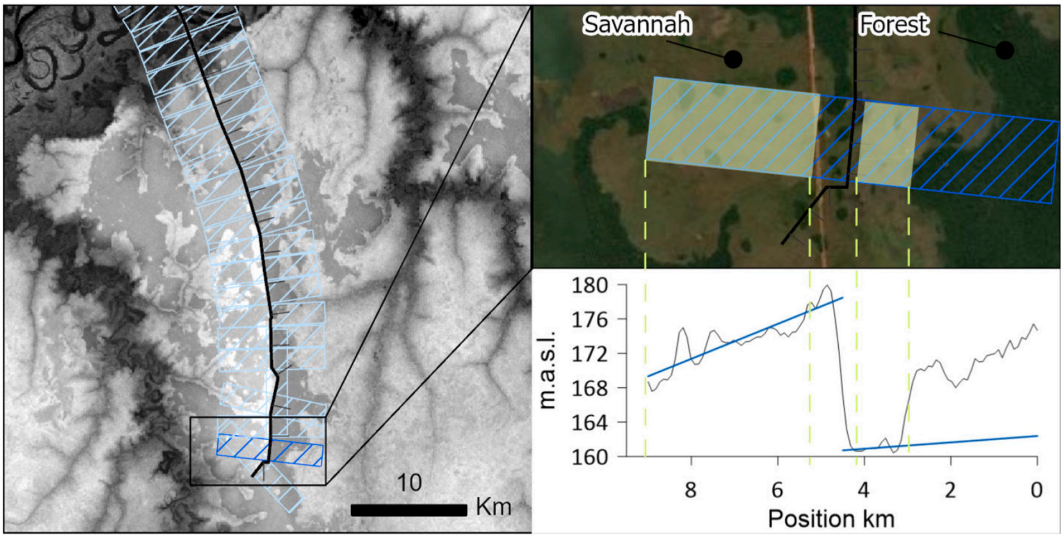

Fig. 5. Example of vertical offset calculation. The solid black line marks the fault with ticks on the downthrown block. The blue lines in the plot are interpolated only on the portion of the profile that correspond to savannah land cover, discarding the forested portion of the profile. In this case (stack number 2 along fault 5 in Fig. 12) the vertical offset is 16 m. (For interpretation of the references to colour in this figure legend, the reader is referred to the web version of this article.)

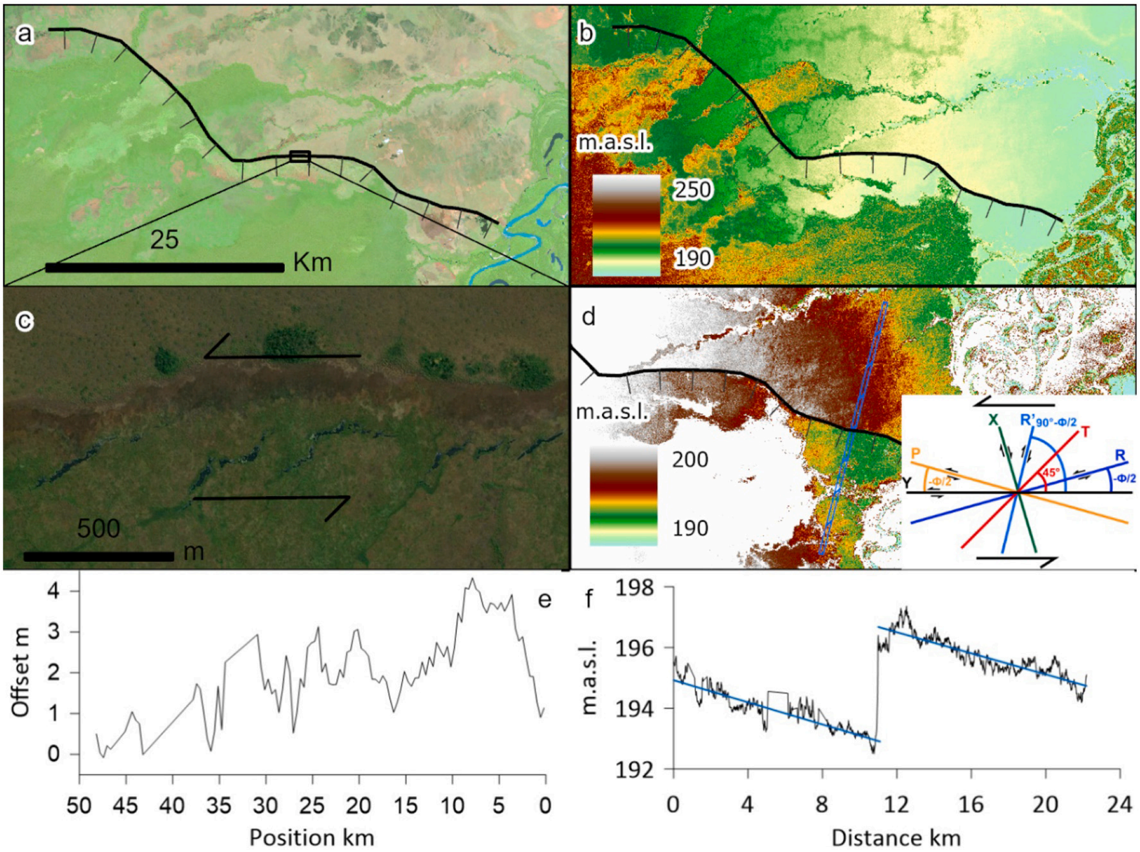

Fig. 6. Fault 1. Panel a shows the fault (solid black line with ticks on the downthrown block) and the land cover, as seen on Landsat imagery, green for forest, pink for savannah. Panel b shows the fault over the digital elevation model. Panel c shows elongated S-shaped lakes formed in what seem to be en-echelon tension fractures, striking 45° with respect to the main fault trend. Panel d shows the digital elevation model with enhanced stretching and the location of the stack used for the topographic profile shown in panel f. The inset shows the direction of Riedel shears (R, R'; Riedel, 1929), X- and Y-shears (X, Y), and tension fractures (T) relative to the main shear zone in a left-lateral setting. Φ is the angle of internal friction. Modified from Bartlett et al. (1981). Panel e shows the along-strike vertical offset measured every 500 m. Panel f shows a topographic profile across the fault. See location in Fig. 2. (For interpretation of the references to colour in this figure legend, the reader is referred to the web version of this article.)

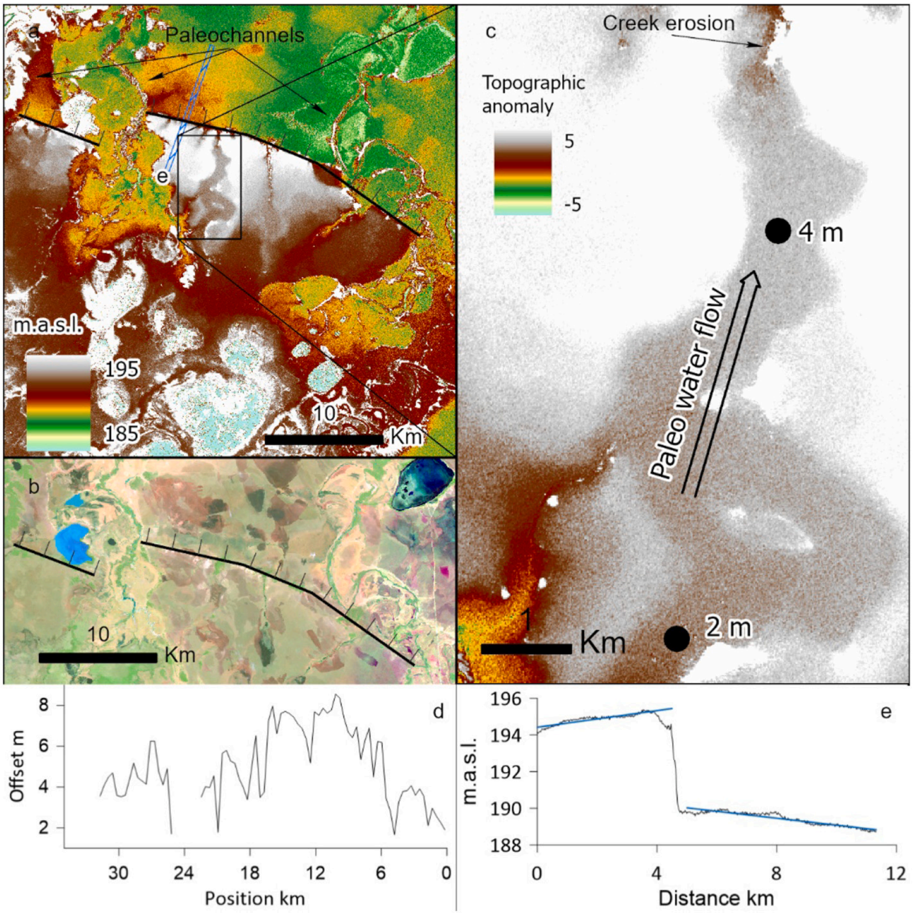

Fig. 7. Fault 2. Panel a shows the NW-SE oriented fault scarp with the Beni paleo-meander belt east of the uplifted block. Panel b shows the fault scarp over the land cover. Panel c, topographic reversal of a paleochannel as seen on the de-trended DEM. In absence of any tectonic movement, the paleochannel in the de-trended image should be horizontal. However, the tilting of the surface caused that its northern part is now 2 m more elevated than it was when the river channel was active. Panel d shows the vertical offset distribution along the fault. Panel e shows the topographic profile across the fault calculated over the blue swath in panel a. See location in Fig. 2. (For interpretation of the references to colour in this figure legend, the reader is referred to the web version of this article.)

Overall, the offset distribution is triangular, but more symmetrical than that of fault 1. The fault crosses a pre-existing paleochannel (Fig. 7). While the general drainage direction of the LM is from south to north, the slope of the paleochannel (Fig. 7c) on the SW block is reversed (towards the SW) due to block tilting. We measure a tilt angle of 0.028° on the SW block. Where the fault crosses the paleochannel, headward erosion within the paleochannel indicates a retreating knickpoint. At this location, both sides of the fault are covered by savannah (Fig. 7b). The southern margin of the uplifted areas has been later eroded by the Beni River. We interpret this fault as a dip-slip fault based on the same criteria as used for fault 1 and the clear backtilt of the footwall.

The third fault (fault 3 in Fig. 2) is located in the centre of the western LM and visible as a 67 km long lineament running NW-SE (Fig. 8). The fault crosses a paleochannel of the Beni River and its scarp faces towards the NE, indicating a tilting of the SW block with uplift of its NE part. The vertical offset is rather constant along the entire length of the fault, with a maximum of 3 m about 15 km from the fault's NW tip. Here, tilting of the SW block caused a slope inversion of the formerly East-draining paleochannel. Consequently, a 15 km long lake formed southwest of the fault (Fig. 8c). A field survey at the site 65.9468140°W; 13.6961780°S revealed that the 3 m vertical displacement is actually distributed across three different fault scarps of about 1 m in height, spaced about 30 m (Fig. 9). This complexity cannot be resolved from the TanDEM-X data. We interpret this fault as a dip-slip fault. Pre-Columbian agricultural fields, raised fields built in order to improve soil drainage (Lombardo et al., 2011), were built along the edge of the upthrown block (Fig. 8e), providing a minimum age of ca. 500 yrs. BP for the fault scarp formation. Upriver from the lake, a small underfit and probably seasonal river flows into the lake. The levees of this small river are still visible inside the lake (Fig. 8d), suggesting that the lake formed after the establishment of this small river and, therefore, also after the abandonment of the channel by the Beni River. Between the lake and the fault, the 12 km long portion of paleochannel is currently being eroded eastward by a creek. Several paleochannels of the Beni River cross faults 2 and 3 (Fig. 10). The faults influenced river planform in two ways: i) changes in river direction when paleochannels cross the fault 2 and ii) changes in the sinuosity index, with an important decrease in sinuosity between fault 2 and 3, probably caused by the slope reduction caused by block tilting. These changes in paths and meandering patterns provide further elements to build a relative chronology of these faults.

The fourth fault is not visible as a distinct scarp because the downthrown eastern side of the fault is occupied by the Mamore River meander belt. Here, the Mamore River goes through a series of compressed meanders followed by asymmetric ones. These meanders, together with a 5 m difference in elevation between the eastern and the western floodplains of the Mamore River, and the presence of rapids already suggested a SSW-NNE oriented fault (Dumont, 1996; Lombardo, 2014). We interpret the structure as a dip-slip fault. Here, the pattern of paleochannel slope reversal and creek incision is repeated. The tilt caused a reversal of the slope of the paleochannel, with a vertical difference of 3 m along 40 km (Fig. 11). The rotation of the block is 0.004°. A creek is eroding along 27 km of the eastern part of the uplifted paleochannel and then drains into the Mamoré River. The tilting of the block is also visible in the paleolevees of the former Beni River. These are buried in correspondence with the downthrown side of the fault 3. The levees gradually rise eastwards and become 5 m higher than their distal back swamps at the upthrown side of fault 4 (Fig. 11). As for the previous fault, the reversal of paleochannel longitudinal profiles formed a 40 km long shallow lake/swamp (Fig. 11b). The two rivers flowing north of the Beni paleochannel, the rivers Omi and the Irunyañez, have a horizontal

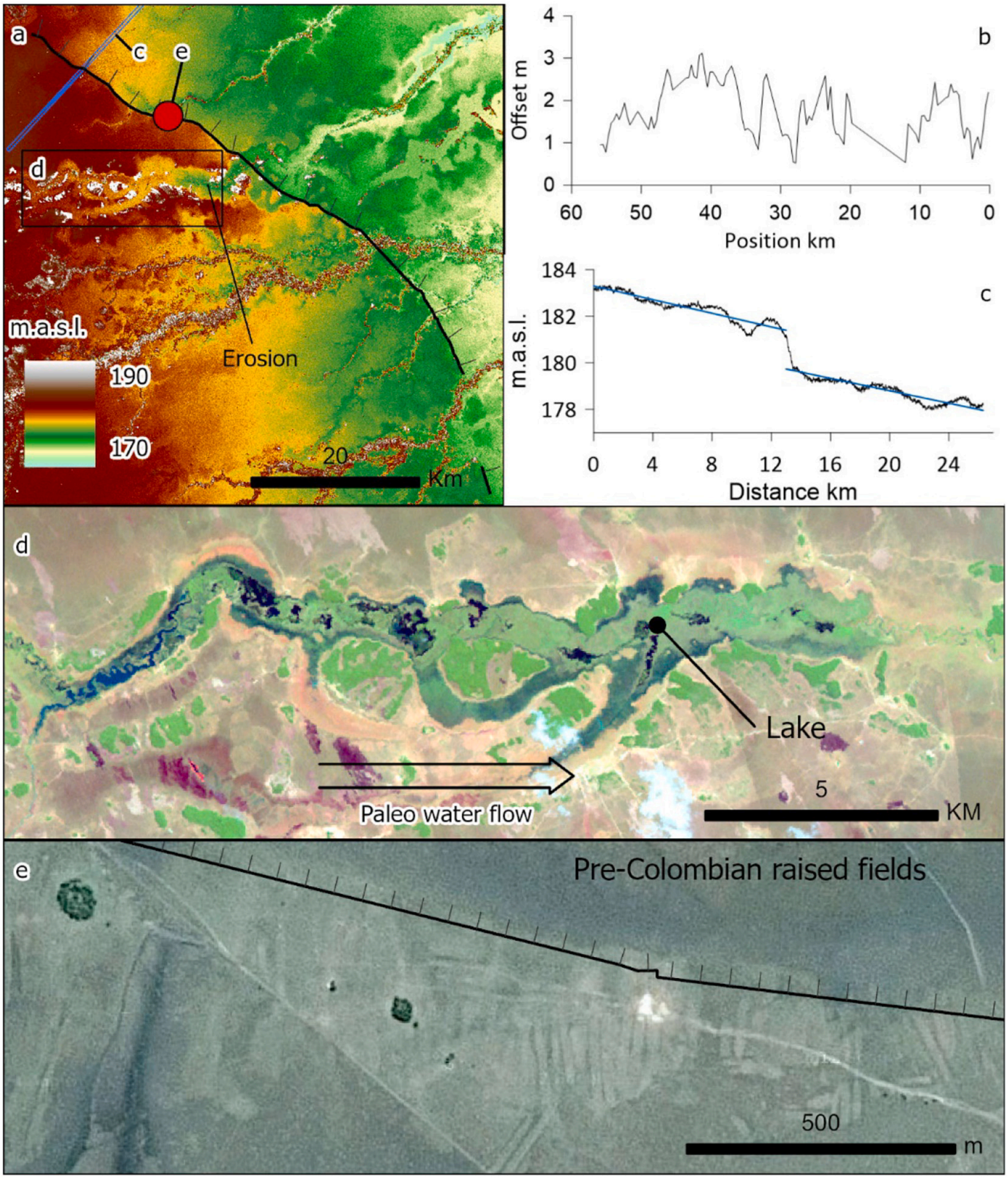

Fig. 8. Fault 3. Panel a shows the NW-SE striking fault scarp. Panel b illustrates the vertical offset along the fault. Panel c shows the topographic profile across the fault, see blue stack in panel a for location. Panel d, lake formed inside the Beni River paleochannel. Panel e shows pre-Columbian raised fields built along the edge of the upthrown block, taking advantage of the improved drainage. See location in Fig. 2. (For interpretation of the references to colour in this figure legend, the reader is referred to the web version of this article.)

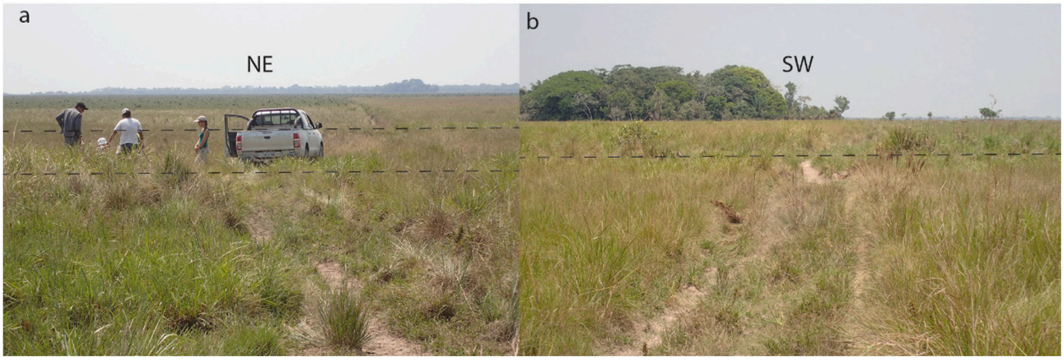

Fig. 9. Fault 3 as seen from the field. In a, view towards NE of two scarps. In b view towards SW of the third scarp.

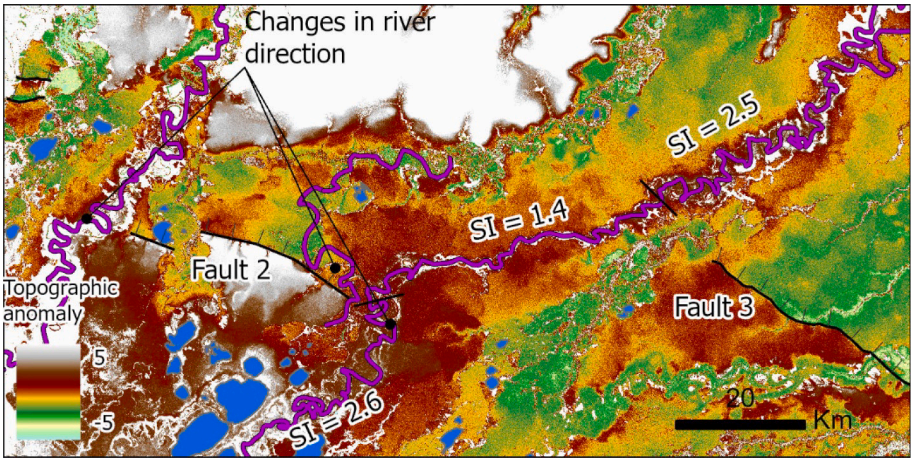

Fig. 10. Changes in rivers planform induced by the faults. Pink lines represent paleochannels of the Beni River. All the paleochannels change direction when crossing fault 2. The southernmost paleochannel has a sharp reduction in sinuosity (SI) when crossing the block between fault 2 and 3, indicating that block tilting reduced the slope. (For interpretation of the references to colour in this figure legend, the reader is referred to the web version of this article.)

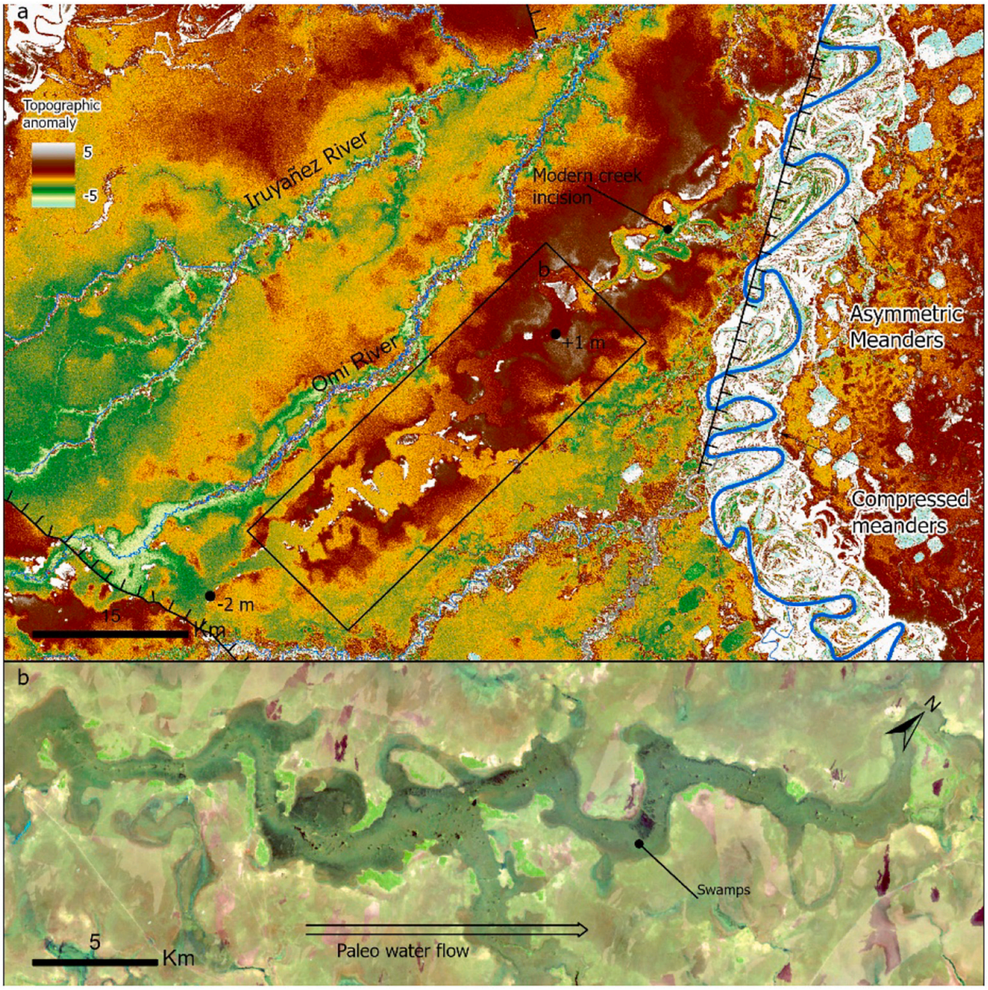

Fig. 11. Fault 4. Panel a shows the de-trended image of the second reversal of the Beni paleochannel. Black line indicates the estimated position of fault 4 with ticks on the downthrown block. In panel b, wetlands formed inside the Beni River paleochannel as seen on a landsat image. See location in Fig. 2.

profile in the de-trended image, indicating that the interpolated trend image correctly represents the general slope of the landscape.

The fifth fault is located north of the Llanos de Moxos, cutting through upland Miocene sediments (Roddaz et al., 2006) that stay well above the seasonal floods (Fig. 12). This 50 km long fault strikes ~NNW-SSE in its northern part and curves to a N-S trend at its southern tip. We measure a maximum vertical offset of 20 m in its southern part, 5 km away from its tip. The offset distribution is rather smooth and triangular,

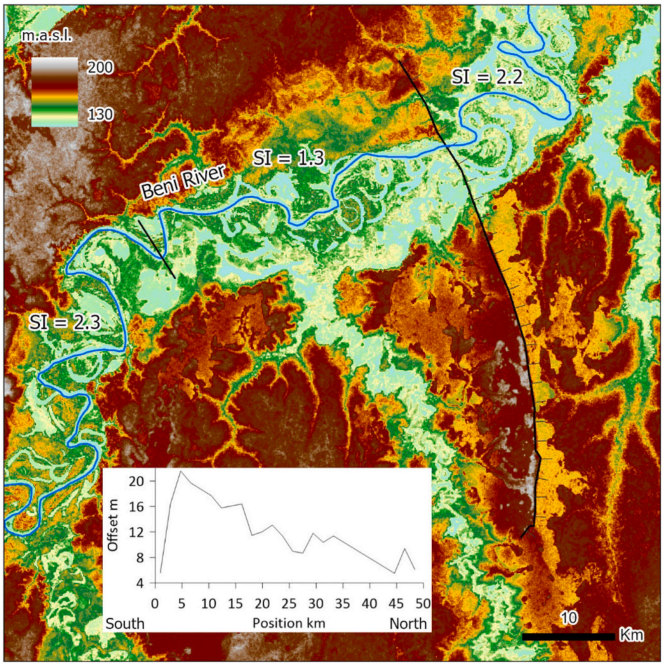

Fig. 12. Fault 5. The inset shows the along fault vertical offset, which reaches a maximum of 20 m. The fault crosses the Beni River, inducing a change in its sinuosity index (SI) from 2.3 to 1.3. See location in Fig. 2.

but skewed to the S. The northern tip of the fault crosses the Beni River. In coincidence with the fault, the river sinuosity drops to 1.3 along a 40 km long upriver segment, which is consistent with a decreasing slope. We interpret fault 5 as a dip-slip fault.

3.2. *Changes induced in the hydrological setting by the faults*

Neotectonics has shaped the river system in the Bolivian Amazon by triggering changes in river planforms and paths (Figs. 10, 12-15).

Dumont (1996) already observed that the Beni and Grande River avulsions were the result of neotectonic movements, with the Beni River being forced to the north by a N-striking fault located between the Pando Block and the Beni River (Figs. 1 and 2). The mechanism for the avulsion of the Mamoré River is less clear. Plotzki et al. (2013) suggested that the Mamoré River avulsion was triggered by an increase in water discharge that happened as a result of climate change towards wetter conditions at around 4 kyrs BP. However, our data suggests that the avulsion of the Mamoré was caused by neotectonics. The de-trended image of the paleochannel and the Mamoré River shows asymmetric backswamps, a variable width of the gallery forest, and changes in the paleo river direction (Fig. 13). These observations suggest a neotectonic influence on the paleo-Mamoré planform. Fig. 14 shows the trend image (the general slope of the LM) with the courses of the modern and paleo Mamoré and Beni Rivers. For both rivers, the paleo-courses follow the steepest slope. In contrast, the modern courses, right after the avulsion points, are orthogonal to the line of maximum slope. This further suggests that the avulsions of both the Beni and Mamoré Rivers were caused by faulting and related tilting of the footwall and hanging wall blocks. Currently, the upper course of the Machupo River, which partly flows inside the Mamoré paleochannel, is getting closer to the Mamoré River. It is only 700 m away from reaching the Mamoré River and potentially triggering a catastrophic avulsion of the Mamoré River into its own paleochannel (Fig. 14). The analysis of the modern Beni and Mamoré Rivers supports the location of the forebulge shown in Aalto et al. (2003) and Roddaz et al. (2006). Both rivers have a drop in sinuosity after entering the forebulge (Fig. 15). The Beni River shows a sharp reduction in meandering after entering the forebulge. In case of the Mamoré River,

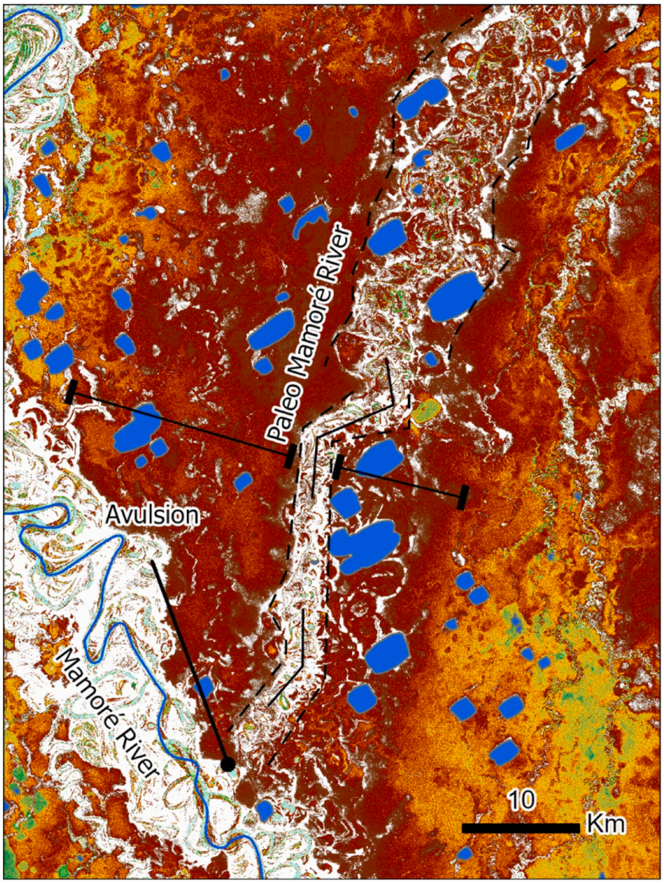

Fig. 13. Detrended image of the Mamoré River avulsion and paleochannel. The paleochannel shows three changes in direction along its first 30 km from the avulsion point along with a thin gallery forest. The backswamps are asymmetric, with the western backswamp being far wider than the eastern one. See location in Fig. 2.

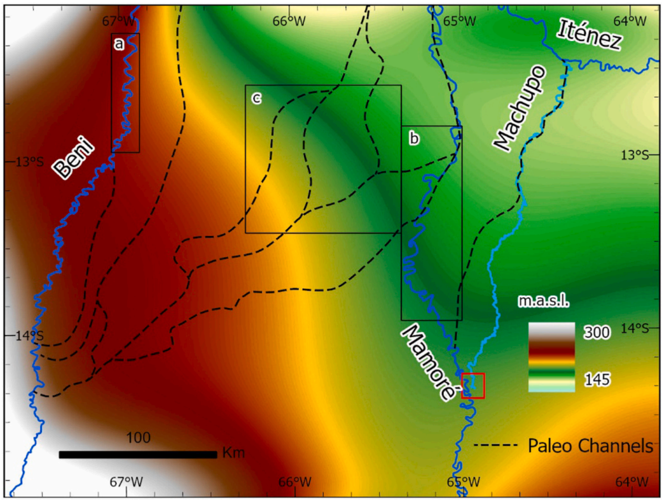

Fig. 14. General topography of the LM derived from the trend image. Major rivers in dark blue, river Machupo in light blue. Dashed lines show the paleochannels of the Beni and Mamoré Rivers. The red square is where the Machupo is about to capture the Mamoré River. Boxes a, b and c indicate the location of panels a, b and c in Fig. 15. (For interpretation of the references to colour in this figure legend, the reader is referred to the web version of this article.)

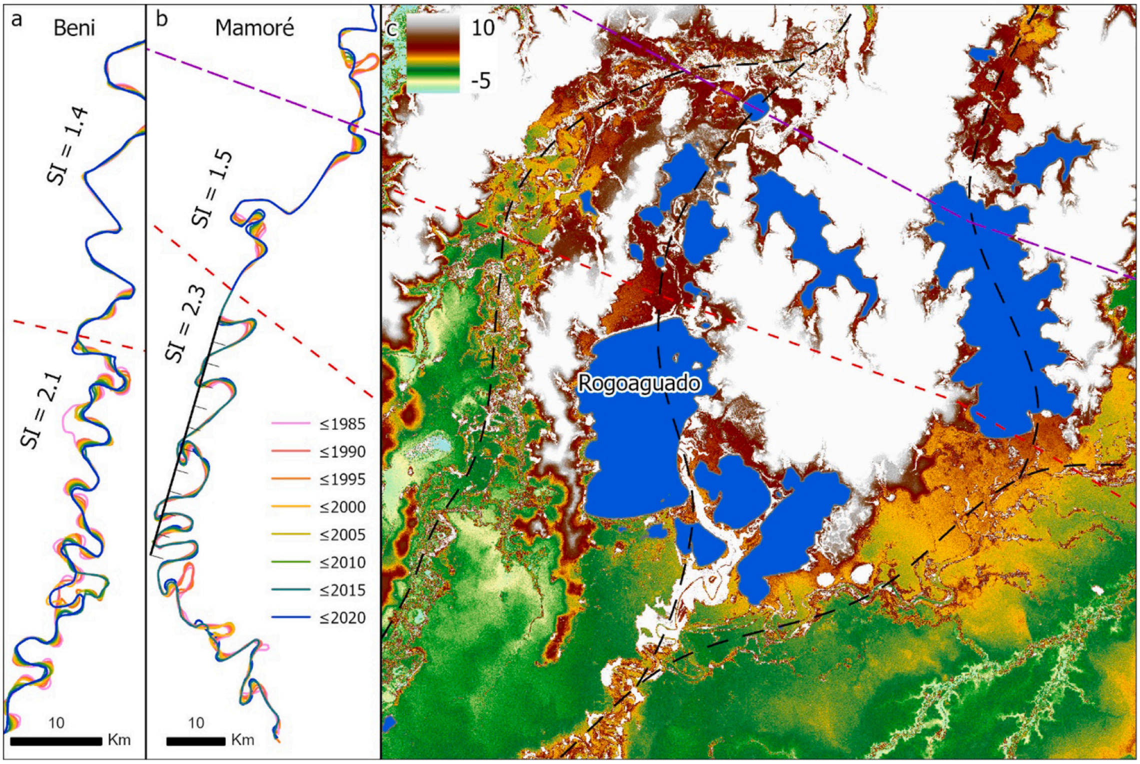

Fig. 15. Effects of the forebulge on the hydrology. The dashed red line indicates the southern boundary of the forebulge based on Aalto et al. (2003); the dashed violet line indicates the axes of the forebulge based on Roddaz et al. (2006). (a) The Beni River shows a drop in meandering and sinuosity after entering the forebulge. (b) The Mamoré River shows compressed and then asymmetric meanders interpreted as resulting from fault 4, followed by a reduction in sinuosity after entering the forebulge. (c), The de-trended image shows positive topographic anomalies north of a group of lakes of tectonic origin, with an inverted profile of 3 paleo courses of the Beni River. Paleo water flow was from south to north. (For interpretation of the references to colour in this figure legend, the reader is referred to the web version of this article.)

the reduction in meandering follows the turns to the right in correspondence with fault 4. Uplift related to the forebulge is also evident in the formation of a group of tectonic lakes in northern Llanos de Moxos (Fig. 15). The difference of the topographic anomalies between the south and the north of lake Rogaguado is about 4.5 m, which roughly coincides with the depth of the water plus the length of the column of lacustrine sediments in lake Rogoaguado (Lombardo, 2014).

4. Discussion

Several studies have used geomorphic evidence to infer neotectonic activity in the Bolivian lowlands (Dumont and Fournier, 1994; Hanagarth, 1993; Lombardo, 2014), however, direct evidence of faulting has been lacking. Here we use digital elevation models to identify the existence of four previously unknown fault scarps in the Bolivian Amazon and provide further data to support the already proposed existence of a fault along the Mamoré River (fault 4). In very active alluvial plains like the LM, fault scarps can be considered very recent features, Pleistocene to Holocene, as fluvial activity tends to erase any surficial evidence of past earthquakes. Hence, they testify to active tectonics.

4.1. Normal or reverse faulting?

The fault scarps that we describe in this study are due to dip-slip faulting, perhaps with a strike-slip component that could explain the en-echelon geometry of s-shaped elongated lakes along the trace of fault 1 (Fig. 6). Both reverse and normal faults could lead to the observed vertical offsets and block tilting.

If faults 1, 2, 3, and 5 were reverse faults in a SW-NE compressional stress field, the most likely mechanism would be a far-field push of the Andes (cf., Bonnemaison et al., 1985; Suárez et al., 1983). The regional stress field indicates (W)SW-(E)NE shortening, although no data are available for our study area (Assumpção et al., 2016; Heidbach et al., 2018; Heidbach et al., 2016). GPS observations (Norabuena et al., 1998) also point to such a stress regime. Räsänen et al. (1992) have argued that the area NW of the LM is characterized by contractional foreland deformation based on the analysis of the fluvial depositional system. An argument in favour of this interpretation is the occurrence of folding and reverse faulting elsewhere east of the Andes (Bellahsen et al., 2016; Bonnemaison et al., 1985; Costa et al., 2000; Costa et al., 1999; Costa et al., 2018; Rimando et al., 2019). For example around 32°S, in the Eastern Sierras Pampeanas in Argentina, shortening is accommodated by reverse faults far from the Andean front (Costa et al., 2021). Similar observations stem from other active orogens worldwide such as the Zagros (e.g., Zebari et al., 2020), the Tien Shan (e.g., Scharer et al., 2004), or the Hindukush/Pamirs (e.g., Gągała et al., 2020; McNab et al., 2019). However, in these settings shortening on reverse faults is mostly accompanied by anticlinal growth and activity on roughly parallel structures. We do not observe this pattern in our study area. Long topographic profiles (Figs. 6-8) across the faults in the LM show pure block tilting, which has been observed as a result of normal faulting in extensional settings in the long term (e.g., Goldsworthy and Jackson, 2000) and in individual earthquakes (e.g., Vittori et al., 2011). Earthquakes on reverse fault often result in folding of the hanging walls (e.g., Lin et al., 2001; Philip and Meghraoui, 1983), which we do not observe here. If the entire study area is under a (W)SW-(E)NE regime of S_{Hmax}, the observed S-shaped lakes along the E-W trending segments of fault 1 could indeed be due to tensile fracturing with a 45° orientation with respect to the main shear zone. In this case the NW-SE striking fault segments should show pure dip-slip, which fits our observations. Sinistral shear on E-W faults is expected in such a stress field, and fault 4 should have a dextral component of motion due to its ~N-S orientation.

Most of the faults may as well include a horizontal component of motion, at least in those segments that are not oriented perpendicular to S_{Hmax}, but we need more data to confirm this. If the NW-SE oriented faults that we describe here were normal faults in an extensional setting, the most plausible mechanism would be extension on top of the flexural forebulge, which underlies the LM (Aalto et al., 2003; Baby et al., 2009; Mora et al., 2009; Roddaz et al., 2006). This interpretation is supported by the shape of the tilted fault blocks as seen in our topographic profiles. No folding is associated with the faults in the LM, but normal faulting would lead to the observed features. An additional argument in favour of normal faulting is the observation that faults 1 and 2 show opposing dip directions, which indicates a graben-like setting. Arguments against normal faulting are the lack of similar structures elsewhere along the forebulge, the location of the faults close to the main deformation front (fault 5 is ~80 km from the anticlines at the NE side of the Andes). Furthermore the faults' location does not fit the inferred trace of the forebulge. The faults described here are located both to the SW and to the NE of the forebulge locations reported in the literature (Aalto et al., 2003; Roddaz et al., 2006). We note, however, that the location of the forebulge is probably not well known because sub-surface data are sparse.

Fault 4 runs perpendicular to the trend of the Andes, but parallel to the SE border of the Fitzcarrald Arch. The load of this topographic high may induce an additional bending moment on the crust that would lead to E-W extension. This could explain normal faulting along fault 4 and fault 5, which is also oriented N-S.

4.2. *Earthquake potential*

Fault 1 has a length of 50 km and a maximum vertical throw of 4 m (Fig. 6). Both the length and the offset could be explained with a single normal faulting earthquake of around magnitude $M_W7.1$, using the empirical relationships between magnitude and rupture length/ maximum offset for normal/all types of faults (Wells and Coppersmith, 1994). A reverse earthquake would give a similar magnitude when looking at the rupture length, but a magnitude of only $M_W6.8$ when using the maximum offset. We note, however, that this latter relationship is prone to very large uncertainties (Wells and Coppersmith, 1994) and we refrain from using it. The offset-to-length ratio of fault 1 is 8×10^{-5} and lies within the typical range of single-earthquakes reported in the literature (10^{-5}–10^{-4}), see review in Kim and Sanderson (2005). The asymmetrical slip distribution might indicate that the fault actually continues further towards the SW and that its surface expression there has been eroded by the Beni River. We carefully analysed the DEMs but did not find any landscape features that would help to solve this. Also, the amount of possible left-lateral motion (Fig. 6c) must remain obscure due to the lack of markers.

Fault 2 is only 25 km long and has a maximum vertical uplift of 8 m. This is an offset-to-length ratio of 3×10^{-4}, which exceeds typical values for single events (Kim and Sanderson, 2005). In case of a single earthquake, the rupture length and the (maximum) offset would correspond to magnitudes of $M_W6.7$ and $M_W7.3$, respectively, using the equations of Wells and Coppersmith (1994) for normal/all types of faults. This discrepancy also indicates that the scarp is a multi-event feature. Additional support comes from the observation that the slip distribution along strike is more symmetrical and that the fault tips are not marked by active rivers. Thus, we probably see the cumulative effect of a number $M_W \sim 6.7$ earthquakes, each of which with typical maximum offsets of ~1.5 m.

The scarp of fault 3 is 67 km long, but only 3 m high. This is an offset-to-length ratio of 4.5×10^{-5}, which would fit a single event (Kim and Sanderson, 2005). Using the empirical relationships of Wells and Coppersmith (1994) for normal faulting quakes and those for all types of events, the length would correspond to earthquakes of $M_W7.2$. The maximum offset would give $M_W7.0$ (normal faulting and all types of earthquakes). Although field evidence shows that the 3 m-high scarp consist of three single steps, the relationship between fault length and offset indicates that this might be a single-event scarp. The slip distribution is rather symmetrical (Fig. 8d). The length of this continuous scarp is unusual. Jackson and Blenkinsop (1997) and subsequent studies point out that the length of normal faults appears to be controlled by the seismogenic thickness of the crust. Our study area is situated where the elastic thickness changes from only 30 km in the west (Tassara et al., 2007) to more than 60 km in the east (Pérez-Gussinyé et al., 2008; Pérez-Gussinyé et al., 2007), but the sparse crustal seismicity does not exceed 35 km depth. We therefore assume that the seismogenic thickness is in the order of 35 km. Thus, the extraordinary long continuous scarp hints to a reverse fault.

Fault 4 is 40 km long and shows a vertical offset of 5 m. We suggest that, similar to fault 1, these values favour a single-event rupture with a magnitude of around M_W7–7.1. Given the regional stress field, the fault could have an unknown component of dextral motion, which we cannot quantify.

The fault located furthest to the NW, fault 5, has a length of 50 km and 20 m maximum vertical offset. This is an offset-to-length ratio of 4 $\times 10^{-4}$, which exceeds typical values for single events (Kim and Sanderson, 2005). Using the rupture length, the empirical relationships of Wells and Coppersmith (1994) for reverse, normal, and all types of earthquakes result in a potential magnitude of $M_W7.1$. The offset, however, would point to very high magnitudes of $M_W7.5$–7.6. Therefore, we interpret this scarp as the result of multiple earthquakes. The fact that the maximum slip was measured close to its southern tip might again hint on a longer fault whose surface expression has been partly removed, but we do not have any subsurface data to further investigate this issue.

Several of the faults discussed here show slip distributions that deviate from the classical bell shape (e.g., Opheim and Gudmundsson, 1989). However, it has become increasingly clear that the slip distribution per earthquake might actually be highly variable (Fletcher et al., 2014; Ghose et al., 1997; McGill and Rubin, 1999) and skewed triangular slip distributions are not uncommon (Barka et al., 2002; Bürgmann et al., 1994; Haeussler et al., 2004; Scholz, 1982). Thus, it is not clear if the asymmetric distribution of vertical offsets really hints to longer faults. Our remote mapping already revealed very long continuous faults, which could be associated with large earthquakes. Furthermore, due to the lack of earthquakes and subsurface data, it must remain uncertain for now if the faults cut the entire seismogenic thickness or if they are, for example, restricted to the upper part of the bending crust as is the case in the oceanic lithosphere (Craig et al., 2014).

The presence of several reversals of paleochannels further suggests that the alluvial plains of the northern LM are affected by several tilting blocks. The tilting is very small, between 10^{-2} and 10^{-3} degrees, but, given the flatness of the landscape in the LM, its effect is notable. No absolute chronology for neotectonics activity is available as yet. Nevertheless, some relative chronologies can be established based on the sequence of events. For example, fault scarp 2 formed after the abandonment of the tilted paleochannel, but before the formation of the Beni paleoriver that eroded the southern margin of the uplifted block (Fig. 7a). Likewise, the age of fault 3 is bracketed by the formation of the lake (Fig. 8d) and the construction of the raised fields (Fig. 8e).

Faults 1–3, located south of the forebulge and roughly with the same NW-SE orientation, can be interpreted as having formed as reverse faults due to SW-NE shortening as a far field effect induced by the Andes, or as normal faults due to the extensional regime between the sub-Andean thrust and the forebulge (Bradley and Kidd, 1991). The latter interpretation is supported by the occurrence of faults with opposing dips that form a graben (faults 1 and 2) and the uplift and tilt of the footwall blocks. The uplift of the forebulge is also consistent with the planform of the rivers Beni and Mamoré and with the uplift responsible for the formation of lakes inside paleo Beni River valleys in the north of the LM (Fig. 12). The Moxos plains are a good example of the type of effects the forebulge induces in alluvial plains. However, the location of the backbulge is here occupied by the Fitzcarrald Arch. This means that the forebulge is not located in between two subsiding basins forming a horst-graben like structure. Instead, the area north of the forebulge is still uplifting.

The uplift of the Fitzcarrald Arch could explain the roughly north-south direction of faults 4 and 5. Subsidence in the LM and uplift in the arch leads to a downbending of the crust towards the east and, thus, to ~E-W extension in the (upper) crust. The Llanos de Moxos is therefore situated in a rather special tectonic setting where the effects of the forebulge and the uplift of the Fitzcarrald Arch due to flat-slab subduction cause multi-directional extension. Although driven by different forces, almost radially divergent extension is for example also documented in SW Turkey (Howell et al., 2017) and leads to a variety of different graben orientations there.

While there is convincing evidence for the uplift of the forebulge and Fitzcarrald Arch to the north, there is no geomorphic expression of the foredeep subsidence along the pre-Andes. Foreland basins are normally deformed by extensional faults that trend parallel to the orogen (Delgado et al., 2012), but in the LM the effect of these faults on the river system seems to be very short lived, being immediately erased by river re-configuration.

Neotectonics had a fundamental role in shaping the modern landscape in the LM. The avulsion of the Mamoré River has been interpreted as resulting from an increase in water discharge (Plotzki et al., 2013). Our data suggest that the Mamoré River could have been pushed westwards by a tilting block. This would explain the “unnatural” counter-clockwise movement of the river that led the Mamoré to leave its path along the line of maximum slope (Fig. 13). The dating of the fluvial sediments and of the beginning of the clay deposition in the paleo Mamoré oxbows could provide a minimum age for the avulsion. It is impossible to estimate the risk of new earthquakes and fault movements at this stage. However, the identification of these five faults allows future paleoseismic studies that can help establish earthquake recurrence intervals. Nevertheless, an important risk can be already identified. The current courses of the Beni and Mamoré Rivers partly flow orthogonal to the line of maximum slope, potentially inducing a clockwise avulsion. This risk seems to be higher for the Mamoré because its course could soon be captured by the Machupo River (a tributary of the Iténez River), which is just 700 m away from reaching the Mamoré meander belt (Fig. 13). The backwards erosion of the Machupo should be closely monitored in order to forecast the moment when the capture could take place. Such a capture would have catastrophic effects for the villages of San Ramón and San Juaquin, which are both established along the Machupo River, and the many private ranches that would be flooded.

Paleoecological reconstructions based on paleobotany have shown important changes in the vegetation in the LM during the Holocene (Lombardo et al., 2019; Mayle et al., 2000), with the most important being an expansion of the rain forest between 4 k - 2 k BP associated to an increase in precipitation. It has been proposed that this climatic shift was responsible for a sharp increase in river avulsions and crevasse splays in the central LM starting around 4 kyrs BP (Lombardo et al., 2018), which shaped the modern landscape of the central and southern LM and the patterns of pre-Columbian human occupation and land use (Lombardo et al., 2015; Lombardo et al., 2012). However, we think that only after a reliable chronology of neotectonics processes has been established, will we be able to identify the relative importance of climate vs. neotectonics in shaping the landscape and landcover of the LM.

The area of the northwestern LM where the fault scarps have been identified is where the highest concentration of anthropogenic forest islands is found (Lombardo et al., 2020). These forest islands are archaeological sites with almost continuous occupation since ca. 10.800 yrs. BP until ca. 2.500 yrs. BP. It is likely that changes in the fluvial network and local drainage caused by block tilting could have changed the local environment of these pre-Columbian populations, with significant effects on the type of resources available. Combining paleoseismic reconstructions with archaeological work could provide new data on societal resilience and human environment interactions in SW Amazonia during the Holocene.

5. Conclusions

Active faults in the Bolivian Amazon, a region currently considered free of seismic risk, have been identified and described. We report on 5 long (between 25 km and 67 km) fault scarps with maximum offsets between 3 and 20 m. These faults have largely controlled the evolution of the landscape of the Bolivian Amazon since the late Pleistocene by i) inducing river avulsions (Figs. 13 and 14) and changes in meandering (Figs. 10 and 15); ii) by changing the local drainage (Fig. 8); and iii) by reversing the slope of river paleochannels and transforming them into lakes (Figs. 11 and 15). The geodynamics of the Bolivian Amazon seems to be characterized by an extensional setting with normal faults driven by the interplay of the subsiding foreland basin and the uplifting of the forebulge and Fitzcarrald arch. An alternative explanation that would fit our data is an overall (W)SW-(E)NE shortening regime, in which case the faults had a reverse mechanism. This is supported by the occurrence of S-shaped lakes on E-W trending fault segments that probably result from tensile fracturing. However, due to the lack of suitable markers, we cannot quantify potential horizontal offsets that would allow deeper insights into these questions. Our study shows that the seismic risk for the local population is not zero. The geometry of the faults suggests earthquakes of very high magnitudes of M_W ranging from 6.7 to 7.6 could have taken place. Even if these earthquakes cause small changes in the regional topography, these can lead to important river avulsions with potentially catastrophic consequences, as it happened during the mid-Holocene when the Mamoré river changed its course. The analysis of the digital elevation model of the Llanos de Moxos shows that the current course of the Mamoré is not the one that goes along the line of maximum slope, suggesting that the Mamoré could soon switch back to its previous course. Absolute chronologies for these faults are currently lacking, but they are very much needed in order to assess the risk of future earthquakes for the local population and to assess to which extent neotectonic processes influenced pre-Columbian settlement patterns and cultural trajectories.

Authors’ Contribution

U.L. conceptualized the research and did the data analyses. U.L. and C.G interpreted the results and wrote the manuscript.

Declaration of Competing Interest

The authors declare that they have no known competing financial interests or personal relationships that could have appeared to influence the work reported in this paper.

Acknowledgements

We thank the Observatorio San Calisto for providing data about recent earthquakes and Caroline de Meyer for her help in identifying fault 5. This work was supported by TerraSAR-X/TanDEM-X mission [grant number DEM_OTHER1040]; the AHRC-FAPESP MoU [grant number AH/S001662/1 (HERCA)]. We thank Leonor Rodrigues and the workers of the Barba Azul Nature Reserve for helping during field reconnaissance of the faults. We thank Francisco Velandia and the anonymous reviewers for their constructive comments, which helped to significantly improve the manuscript. Jeremy Rimando provided very helpful comments on an earlier version of the manuscript.

References

Aalto, R., et al., 2003. Episodic sediment accumulation on Amazonian flood plains influenced by El Niño/Southern Oscillation. Nature 425 (6957), 493–497.

Antonijevic, S.K., et al., 2015. The role of ridges in the formation and longevity of flat slabs. Nature 524 (7564), 212–215.

Assumpção, M., Dias, F.L., Zevallos, I., Naliboff, J.B., 2016. Intraplate stress field in South America from earthquake focal mechanisms. J. S. Am. Earth Sci. 71, 278–295.

Axen, G.J., van Wijk, J.W., Currie, C.A., 2018. Basal continental mantle lithosphere displaced by flat-slab subduction. Nat. Geosci. 11 (12), 961–964.

Baby, P., Guyot, J.L., Hérail, G., 2009. Tectonic Control of Erosion and Sedimentation in the Amazon Basin of Bolivia, vol. 23, pp. 3225–3229 (22).

Barka, A., et al., 2002. The surface rupture and slip distribution of the 17 August 1999 Izmit earthquake (M 7.4), North Anatolian fault. Bull. Seismol. Soc. Am. 92 (1), 43–60.

Bartlett, W.L., Friedman, M., Logan, J.M., 1981. Experimental folding and faulting of rocks under confining pressure part IX. Wrench faults in limestone layers. Tectonophysics 79 (3), 255–277.

Bellahsen, N., Sebrier, M., Siame, L., 2016. Crustal shortening at the Sierra Pie de Palo (Sierras Pampeanas, Argentina): near-surface basement folding and thrusting. Geol. Mag. 153 (5–6), 992–1012.

Berryman, K.R., et al., 2012. Major Earthquakes Occur Regularly on an Isolated Plate Boundary Fault, vol. 336, pp. 1690–1693 (6089).

Bishop, B.T., et al., 2017. Causes and consequences of flat-slab subduction in southern Peru. Geosphere 13 (5), 1392–1407.

Bishop, B.T., et al., 2018. Foreland uplift during flat subduction: Insights from the Peruvian Andes and Fitzcarrald Arch. Tectonophysics 731-732, 73–84.

Bonnemaison, M., et al., 1985. Evolucion geomorfologica y placeres de oro en los Andes surorientales del Peru. Boletin de la Sociedad Geologica del Peru 75, 13–32.

Bradley, D.C., Kidd, W.S.F., 1991. Flexural extension of the upper continental crust in collisional foredeeps. GSA Bull. 103 (11), 1416–1438.

Bürgmann, R., Pollard, D.D., Martel, S.J., 1994. Slip distributions on faults: effects of stress gradients, inelastic deformation, heterogeneous host-rock stiffness, and fault interaction. J. Struct. Geol. 16 (12), 1675–1690.

Choi, J.-H., et al., 2018. Geologic Inheritance and Earthquake Rupture Processes: the 1905 $M \geq 8$ Tsetserleg-Bulnay Strike-Slip Earthquake Sequence, Mongolia, vol. 123, pp. 1925–1953 (2).

Costa, C., et al., 2000. Map and database of Quaternary faults and folds in Argentina (2000-108).

Costa, C.H., Giaccardi, A.D., González Díaz, E.F., 1999. Palaeolandsurfaces and Neotectonic Analysis in the Southern Sierras Pampeanas, Argentina, vol. 162, pp. 229–238 (1).

Costa, C.H., Owen, L.A., Ricci, W.R., Johnson, W.J., Halperin, A.D., 2018. Holocene activity and seismogenic capability of intraplate thrusts: Insights from the Pampean Ranges, Argentina. Tectonophysics 737, 57–70.

Costa, C.H., Owen, L.A., Johnson, W.J., Kirby, E., 2021. Quaternary activity and seismogenic potential of the Sierra Chica Fault System, Pampean Ranges of Argentina. J. S. Am. Earth Sci. 110, 103328.

Craig, T.J., Copley, A., Jackson, J., 2014. A reassessment of outer-rise seismicity and its implications for the mechanics of oceanic lithosphere. Geophys. J. Int. 197 (1), 63–89.

DeCelles, P.G., Giles, K.A., 1996. Foreland basin systems. Basin Res. 8 (2), 105–123.

Delgado, A., Mora, A., Reyes-Harker, A., 2012. Deformation partitioning in the Llanos foreland basin during the Cenozoic and its correlation with mountain building in the hinterland. J. S. Am. Earth Sci. 39, 228–244.

Dumont, J.F., 1996. Neotectonics of the Subandes-Brazilian craton boundary using geomorphological data: the Marañon and Beni basins. Tectonophysics 257, 137–151.

Dumont, J.F., Fournier, M., 1994. Geodynamic environment of Quaternary morphostructures of the subandean foreland basins of Peru and Bolivia: Characteristics and study methods. Quat. Int. 21, 129–142.

Dziewonski, A.M., Chou, T.-A., Woodhouse, J.H., 1981. Determination of Earthquake Source Parameters From Waveform Data for Studies of Global and Regional Seismicity, vol. 86, pp. 2825–2852 (B4).

Ekström, G., Nettles, M., Dziewoński, A.M., 2012. The global CMT project 2004–2010: Centroid-moment tensors for 13,017 earthquakes. Phys. Earth Planet. Inter. 200-201, 1–9.

El Hamdouni, R., Irigaray, C., Fernández, T., Chacón, J., Keller, E.A., 2008. Assessment of relative active tectonics, southwest border of the Sierra Nevada (southern Spain). Geomorphology 96 (1), 150–173.

Esch, T., et al., 2012. TanDEM-X mission-new perspectives for the inventory and monitoring of global settlement patterns. J. Appl. Remote. Sens. 1, 061702.

Espurt, N., et al., 2007. How does the Nazca Ridge subduction influence the modern Amazonian foreland basin? Geology 35 (6), 515–518.

Fletcher, J.M., et al., 2014. Assembly of a large earthquake from a complex fault system: Surface rupture kinematics of the 4 April 2010 El Mayor–Cucapah (Mexico) Mw 7.2 earthquake. Geosphere 10 (4), 797–827.

Fuller, M.L., 1988. The New Madrid Earthquake, 494. Central United States Earthquake Consortium.

Gągała, Ł., et al., 2020. Tajik Basin and Southwestern Tian Shan, Northwestern India-Asia Collision Zone: 1. Structure, Kinematics, and Salt Tectonics in the Tajik Fold-and-Thrust Belt of the Western Foreland of the Pamir, vol. 39 (5). e2019TC005871.

Ghose, S., et al., 1997. The MS = 7.3 1992 Suusamyr, Kyrgyzstan, earthquake in the tien Shan: 2. Aftershock focal mechanisms and surface deformation. Bull. Seismol. Soc. Am. 87 (1), 23–38.

Goldsworthy, M., Jackson, J., 2000. Active normal fault evolution in Greece revealed by geomorphology and drainage patterns. J. Geol. Soc. 157 (5), 967–981.

Gómez, J., Schobbenhaus, C., Montes, N.E., 2019. Geological Map of South America 2019. Scale 1:5 000 000. Commission for the Geological Map of the World (CGMW), Colombian Geological Survey, and Geological Survey of Brazil, Paris.

Grützner, C., et al., 2017. Assessing the activity of faults in continental interiors: Palaeoseismic insights from SE Kazakhstan. Earth Planet. Sci. Lett. 459, 93–104.

Haeussler, P.J., et al., 2004. Surface rupture and slip distribution of the Denali and Totschunda faults in the 3 November 2002 M 7.9 earthquake, Alaska. Bull. Seismol. Soc. Am. 94 (6B), S23–S52.

Hanagarth, W., 1993. Acerca de la geoecología de las sabanas del Beni en el noreste de Bolivia. Instituto de ecología, La Paz.

Heidbach, O., Rajabi, M., Reiter, K., Ziegler, M.O., Team, W., 2016. In: Services, G.D. (Ed.), World Stress Map Database Release 2016.

Heidbach, O., et al., 2018. The World stress Map database release 2016: Crustal stress pattern across scales. Tectonophysics 744, 484–498.

Howell, A., Jackson, J., Copley, A., McKenzie, D., Nissen, E., 2017. Subduction and vertical coastal motions in the eastern Mediterranean. Geophys. J. Int. 211 (1), 593–620.

Jackson, J., Blenkinsop, T., 1997. The Bilila-Mtakataka fault in Malaŵi: An Active, 100-km Long, Normal Fault Segment in Thick Seismogenic Crust, vol. 16, pp. 137–150 (1).

Junk, W., 2013. Current state of knowledge regarding South American wetlands and their future under global climate change. Aquat. Sci. Res. Across Bound. 75 (1), 113–131.

Kim, Y.-S., Sanderson, D.J., 2005. The relationship between displacement and length of faults: a review. Earth Sci. Rev. 68 (3), 317–334.

Leprince, S., Barbot, S., Ayoub, F., Avouac, J., 2007. Automatic and precise orthorectification, coregistration, and subpixel correlation of satellite images, application to ground deformation measurements. IEEE Trans. Geosci. Remote Sens. 45 (6), 1529–1558.

Lin, A., Ouchi, T., Chen, A., Maruyama, T., 2001. Co-seismic displacements, folding and shortening structures along the Chelungpu surface rupture zone occurred during the 1999 Chi-Chi (Taiwan) earthquake. Tectonophysics 330 (3), 225–244.

Lin, A., Guo, J., Kano, K.-i. and Awata, Y., 2006. Average slip rate and recurrence interval of large-magnitude earthquakes on the western segment of the strike-slip kunlun fault, Northern Tibet. Bull. Seismol. Soc. Am. 96 (5), 1597–1611.

Lombardo, U., 2014. Neotectonics, flooding patterns and landscape evolution in southern Amazonia. Earth Surf. Dynam. 2 (2), 493–511.

Lombardo, U., 2016. Alluvial plain dynamics in the southern Amazonian foreland basin. Earth Syst. Dynam. 7 (2), 453–467.

Lombardo, U., Canal-Beeby, E., Fehr, S., Veit, H., 2011. Raised fields in the Bolivian Amazonia: a prehistoric green revolution or a flood risk mitigation strategy? J. Archaeol. Sci. 38 (3), 502–512.

Lombardo, U., May, J.-H., Veit, H., 2012. Mid- to late-Holocene fluvial activity behind pre-Columbian social complexity in the southwestern Amazon basin. The Holocene 22 (9), 1035–1045.

Lombardo, U., Denier, S., Veit, H., 2015. Soil properties and pre-Columbian settlement patterns in the Monumental Mounds Region of the Llanos de Moxos, Bolivian Amazon. SOIL 1 (1), 65–81.

Lombardo, U., Rodrigues, L., Veit, H., 2018. Alluvial plain dynamics and human occupation in SW Amazonia during the Holocene: a paleosol-based reconstruction. Quat. Sci. Rev. 180, 30–41.

Lombardo, U., et al., 2019. Holocene land cover change in South-Western Amazonia inferred from paleoflood archives. Glob. Planet. Chang. 174, 105–114.

Lombardo, U., et al., 2020. Early Holocene crop cultivation and landscape modification in Amazonia. Nature. 581 (7807), 190–195.

Mayle, F.E., Burbridge, R., Killeen, T.J., 2000. Millennial-scale dynamics of southern Amazonian rain forests. Science 290 (5500), 2291–2294.

McGill, S.F., Rubin, C.M., 1999. Surficial Slip Distribution on the Central Emerson Fault During the June 28, 1992, Landers Earthquake, California, vol. 104, pp. 4811–4833 (B3).

McNab, F., Sloan, R.A., Walker, R.T., 2019. Simultaneous orthogonal shortening in the Afghan-Tajik Depression. Geology 47 (9), 862–866.

Mora, A., et al., 2009. Tectonic History of the Andes and Sub-Andean Zones: Implications for the Development of the Amazon Drainage Basin, Amazonia: Landscape and Species Evolution, pp. 38–60.

Norabuena, E., et al., 1998. Space geodetic observations of Nazca-South America convergence across the Central Andes. Science 279 (5349), 358–362.

Observatorio_San_Calixto, . Mapa probabilistico de amenaza sismica para Bolivia (PHSBO - 2019). https://www.osc.org.bo/index.php/es/sismicidad/mapa-amenaza. Observatorio_San_Calixto, La Paz.

Opheim, J.A., Gudmundsson, A., 1989. Formation and geometry of fractures, and related volcanism, of the Krafla fissure swarm, Northeast Iceland. GSA Bull. 101 (12), 1608–1622.

Pérez-Gussinyé, M., Lowry, A.R., Watts, A.B., 2007. Effective Elastic Thickness of South America and its Implications for Intracontinental Deformation, vol. 8 (5).

Pérez-Gussinyé, M., Lowry, A.R., Phipps Morgan, J., Tassara, A., 2008. Effective Elastic Thickness Variations Along the Andean Margin and Their Relationship to Subduction Geometry, vol. 9 (2).

Philip, H., Meghraoui, M., 1983. Structural Analysis and Interpretation of the Surface Deformations of the El Asnam Earthquake of October 10, 1980, vol. 2, pp. 17–49 (1).

Plafker, G., 1964. Oriented lakes and lineaments of northeastern Bolivia. Geol. Soc. Am. Bull. 75 (6), 503–522.

Plotzki, A., May, J.H., Preusser, F., Veit, H., 2013. Geomorphological and sedimentary evidence for late Pleistocene to Holocene hydrological change along the Río Mamoré, Bolivian Amazon. J. S. Am. Earth Sci. 47, 230–242.

Quigley, M., et al., 2010. Surface rupture of the Greendale fault during the MW 7. 1 Darfield (Canterbury) earthquake, New Zealand: initial findings. Bull. N. Z. Soc. Earthq. Eng. 43 (4).

Räsänen, M., Neller, R., Salo, J., Jungner, H., 1992. Recent and ancient fluvial deposition systems in the Amazonian foreland basin, Peru. Geol. Mag. 129 (3), 293–306.

Regard, V., et al., 2009. Geomorphic evidence for recent uplift of the Fitzcarrald Arch (Peru): a response to the Nazca Ridge subduction. Geomorphology 107 (3–4), 107–117.

Riedel, W., 1929. Zur Mechanik geologischer Brucherscheinungen ein Beitrag zum Problem der Fiederspalten. Zentbl. Miner. Geol. Palaont Abt. B 8, 354–368.

Rimando, J.M., et al., 2019. Late Quaternary Activity of the La Rinconada Fault Zone, San Juan, Argentina, vol. 38, pp. 916–940 (3).

Roddaz, M., Viers, J., Brusset, S., Baby, P., Hérail, G., 2005. Sediment provenances and drainage evolution of the Neogene Amazonian foreland basin. Earth Planet. Sci. Lett. 239 (1–2), 57–78.

Roddaz, M., Brusset, S., Baby, P., Herail, G., 2006. Miocene tidal-influenced sedimentation to continental Pliocene sedimentation in the forebulge–backbulge depozones of the Beni–Mamore foreland Basin (northern Bolivia). J. S. Am. Earth Sci. 20 (4), 351–368.

Scharer, K.M., et al., 2004. Detachment folding in the Southwestern Tian Shan–Tarim foreland, China: shortening estimates and rates. J. Struct. Geol. 26 (11), 2119–2137.

Scholz, C.H., 1982. Scaling laws for large earthquakes: Consequences for physical models. Bull. Seismol. Soc. Am. 72 (1), 1–14.

Schumm, S.A., Dumont, J.F., Holbrook, J.M., 2002. Active Tectonics and Alluvial Rivers. Cambridge University Press.

Shen, T., Rogozhin, E.A., 2018. Geodynamic and Seismotectonic activity in Eastern Tibet in the 21st Century. Seism. Instrum. 54 (4), 461–478.

Smith, N.D., McCarthy, T.S., Ellery, W.N., Merry, C.L., Rüther, H., 1997. Avulsion and anastomosis in the panhandle region of the Okavango Fan, Botswana. Geomorphology 20 (1), 49–65.

Snyder, N.P., Whipple, K.X., Tucker, G.E., Merritts, D.J., 2000. Landscape response to tectonic forcing: Digital elevation model analysis of stream profiles in the Mendocino triple junction region, northern California. GSA Bull. 112 (8), 1250–1263.

Suárez, G., Molnar, P., Burchfiel, B.C., 1983. Seismicity, Fault Plane Solutions, Depth of Faulting, and Active Tectonics of the Andes of Peru, Ecuador, and Southern Colombia, vol. 88, pp. 10403–10428 (B12).

Swan III, F.H., Schwartz, D.P., Cluff, L.S., 1980. Recurrence of moderate to large magnitude earthquakes produced by surface faulting on the Wasatch fault zone, Utah. Bull. Seismol. Soc. Am. 70 (5), 1431–1462.

Tassara, A., Swain, C., Hackney, R., Kirby, J., 2007. Elastic thickness structure of South America estimated using wavelets and satellite-derived gravity data. Earth Planet. Sci. Lett. 253 (1), 17–36.

Tchalenko, J.S., 1970. Similarities between Shear zones of Different Magnitudes. Geol. Soc. Am. Bull. 81 (6), 1625–1640.

Tchalenko, J.S., Ambraseys, N.N., 1970. Structural analysis of the Dasht-e Bayaz (Iran) earthquake fractures. Geol. Soc. Am. Bull. 81 (1), 41–60.

Timár, G., Sümegi, P., Horváth, F., 2005. Late Quaternary dynamics of the Tisza River: evidence of climatic and tectonic controls. Tectonophysics 410 (1), 97–110.

USGS, 2020. Earthquake Facts and Statistics. https://earthquake.usgs.gov/earthquakes/browse/stats.php.

Vittori, E., et al., 2011. Surface Faulting of the 6 April 2009 Mw 6.3 L'Aquila Earthquake in Central Italy. Bull. Seismol. Soc. Am. 101 (4), 1507–1530.

Wells, D.L., Coppersmith, K.J., 1994. New empirical relationships among magnitude, rupture length, rupture width, rupture area, and surface displacement. Bull. Seismol. Soc. Am. 84 (4), 974–1002.

Zebari, M., et al., 2020. Structural style of the NW Zagros Mountains and the role of basement thrusting for its Mountain Front Flexure, Kurdistan Region of Iraq. J. Struct. Geol. 141, 104206.

Zhang, S., et al., 2020. A new method for supporting interpretation of paleochannels in a large scale — Detrended Digital Elevation Model Interpretation. Geomorphology 369, 107374.